H1prelim-09-035 Submitted to

XVII International Workshop on Deep Inelastic Scattering, DIS2009, April 26-30, 2009, Madrid
Parallel Session **Hadronic final states and QCD**

Electronic Access: www-h1.desy.de/publications/H1preliminary.short_list.html

Prompt photons in photoproduction at HERA

H1 Collaboration

Abstract

A measurement of the production of prompt photons in photoproduction by the H1 experiment at HERA is presented. The analysis is based on the data taken in the years 2004-2007, with a total integrated luminosity of 340 pb^{-1}. Prompt photon cross sections are measured for photons with a transverse energy in the range $6 < E_T^\gamma < 15\,\text{GeV}$ and in the pseudorapidity range $-1.0 < \eta^\gamma < 2.43$. Cross sections for prompt photon events with an additional hadronic jet are measured as a function of the transverse energy and pseudorapidity of the jet and of the momentum fractions x_γ and x_p of the incident photon and proton, respectively, carried by the constituents participating in the hard scattering process. Additionally, the transverse correlation between the photon and the jet is studied. The results are compared with predictions of a next-to-leading order calculation and a calculation based on the k_T factorisation approach.

1 Introduction

Events with an isolated photon emerging from the hard subprocess $ep \to e\gamma X$, so called prompt photons, are a powerful probe of the dynamics of the hard subprocess. They require generally lower corrections for hadronisation than measurements relying on jets, since the photons emerge without the hadronisation process by which final state quarks or gluons form a jet. Production of isolated photons with high transverse momentum can be calculated in perturbation theory, but previous measurements have shown that higher order Quantum Chromodynamics (QCD) corrections are important.

High energy electron-proton scattering, as it has been carried out at the ep collider HERA, is dominated by so-called photoproduction processes. The beam lepton emits a quasi real photon which either interacts directly with the proton (”direct process”) or resolves into partons which engage in the hard scattering process (”resolved process”).

This paper presents a measurement of prompt photon production in photoproduction. The data used for the measurement have been collected by the H1 detector in the years $2004 - 2007$ with a total luminosity of 340 pb^{-1}. This corresponds to an increase by a factor of three compared to the previous measurement [1]. Isolated photons with transverse energy $6 < E_T^\gamma < 15$ GeV and pseudorapidity $-1.0 < \eta^\gamma < 2.43$ are selected in events with inelasticity $0.1 < y < 0.7$. This extends the phase space of previous measurements at HERA towards larger pseudorapidities of the photon and to lower event inelasticities.

2 Theoretical Predictions

Prompt photon production is calculated in NLO QCD calculations and in the k_T factorisation approach.

The full NLO calculation by Fontannaz, Guillet and Heinrich (FGH) [2, 3] includes the leading order direct and resolved processes $\gamma q \to \gamma q$, and NLO corrections to these terms. In resolved events the photon emitted by the electron fluctuates into a hadronic state and a parton of this hadronic state takes part in the hard interaction. Besides the direct hard interaction, photons may also be produced from the fragmentation of a high p_T quark or gluon in the final state. The fragmentation process, described by a fragmentation function, is included in the calculation as well as the direct box diagram $\gamma g \to \gamma g$. The latter is calculated to order α_s^2. The calculation uses the parton density functions CTEQ6 [4] for the proton and AFG04 [5] for the photon. The renormalisation μ_R, factorisation μ_F, and fragmentation μ_f scales are chosen to be $\mu_R = \mu_F = \mu_f = p_T^\gamma$.

The predictions of A. Lipatov and N. Zotov (LZ) [6] are based on the k_T factorisation approach. The calculation uses the unintegrated quark and gluon densities of the photon and the proton using the Kimber-Martin-Ryskin (KMR) prescription [7] with the GRV parameterisations of the collinear quark and gluon densities [8, 9]. This KMR procedure is expected to account for the main part of the collinear higher order QCD corrections [6]. Direct and resolved processes are considered in the calculation, the contributions from fragmentation and from the box diagram are neglected.

The LO Monte Carlo (MC) generator PYTHIA 6.2 [10] is used in this analysis for the prediction of the signal and background distributions. The simulations use the parton densities CTEQ6L [4] for the proton and SASG-1D [11] for the photon. The simulated signal contains contributions from direct and resolved production of prompt photons as well as from photons radiated by the quark in di-jet events.

Background to the analysis of prompt photons mainly arises from decay photons of hadrons in photoproduction events, like π^0 and η, which contribute to more than 90%. Direct and resolved photoproduction of di-jet events is simulated by PYTHIA. Events with a high energetic photon radiated from the quark are removed from the background sample and included in the radiated signal component.

All generated events are passed through the full GEANT [12] based simulation of the H1 detector which takes into account the different data taking periods, and are subject to the same reconstruction and analysis chain as the data.

3 Experimental Method

3.1 Event Selection

The data were collected with the H1 [13] detector at HERA in the years $2004 - 2007$. During this period HERA collided positrons or electrons [1] of energy $E_e = 27.5$ GeV with protons of energy $E_p = 920$ GeV corresponding to a centre-of-mass energy of $\sqrt{s} = 319$ GeV. The data sample of this analysis corresponds to an integrated luminosity of $340\ \mathrm{pb}^{-1}$.

Events are selected with a photon candidate in the LAr calorimeter of transverse energy $6 < E_T^\gamma < 15.0$ GeV and pseudorapidity $-1. < \eta^\gamma < 2.4$. Photon candidates are defined as electromagnetic cluster in the LAr calorimeter with no track signal assigned to it.

Neutral current deep-inelastic scattering (DIS) events are suppressed by rejecting events with an electron candidate not previously identified as photon candidate. This restricts the virtuality of the incident photon to the range $Q^2 < 4$ GeV^2. The inelasticity y_h is evaluated as $y_h = \Sigma(E - p_z)/2E_e$, where the sum runs over all measured final state particles with energy (E) and longitudinal momentum (p_z). The inelasticity is restricted to $0.1 < y_h < 0.7$. The cut at low y_h removes residual beam gas background and the higher cut on y_h removes background from DIS events including DIS events with the electron misidentified as a photon.

In order to remove background events from non-ep sources, at least two tracks are required in the central tracker, assuring a good reconstruction of the longitudinal event vertex which is required to be within 40 cm around the nominal interaction point.

The transverse radius R_T of the photon candidate cluster is required to be smaller than 6 cm. This cut on the transverse size of the cluster removes background from neutral hadrons

[1] The analysis uses data from periods when the beam lepton was either a positron or an electron. Unless otherwise stated, the term electron refers to both the electron and the positron.

that decay into multiple photons. In most cases such decay photons are merged into one electromagnetic cluster, which tends to have a wider transverse distribution than that of a single photon.

Tracks and calorimeter energy deposits not previously identified as photon candidate are used to form combined cluster-track objects. The photon candidate and the cluster-track objects are combined into massless jets using an inclusive k_T algorithm [14]. Jets are reconstructed in the pseudorapidity range $-2.0 < \eta^{\text{jet}} < 3.0$ with a transverse momentum of $p_T^{\text{jet}} > 3.0$ GeV. Due to the harder kinematical cuts for the photon candidate there is always a jet containing the photon candidate, called the photon-jet. All other jets are classified as hadronic jets. To ensure isolation of the photon, the fraction $z = E_T^{\gamma}/E_T^{\gamma-\text{jet}}$ of the transverse energy of the photon-jet carried by the photon candidate has to be larger than 90%. This isolation requirement largely suppresses background from photons produced in the hadron decay cascade. Only events with exactly one isolated photon candidate are accepted.

For the exclusive sample, events are selected with a photon candidate accompanied by a hadronic jet with $p_T^{\text{jet}} > 4.5$ GeV and $-1.3 < \eta^{\text{jet}} < 2.3$. If more than one jet is found within the kinematic cuts, the jet with the highest p_T^{jet} is accepted.

Four additional observables are defined for the exclusive sample which give more insight in the underlying partonic process:

- The estimators x_γ^{LO} and x_p^{LO}, which in LO correspond to the longitudinal momentum fractions of the partons in the photon and the proton, respectively, are defined as

$$x_\gamma^{LO} = E_T^{\gamma}(e^{-\eta^{\text{jet}}} + e^{-\eta^{\gamma}})/(2yE_e) \tag{1}$$

  and

$$x_p^{LO} = E_T^{\gamma}(e^{\eta^{\text{jet}}} + e^{\eta^{\gamma}})/(2E_p). \tag{2}$$

- $p_\perp$ and $\Delta\Phi$ are two observables describing the transverse correlation between the photon and the jet. $\Delta\Phi$ is the azimuthal acoplanarity between the photon and the jet and $p_\perp$ is the photon momentum perpendicular to the jet direction in the transverse plane

$$p_\perp \equiv \frac{|\ \vec{p}_T^{\,\gamma} \times \vec{p}_T^{\,jet}\ |}{|\ \vec{p}_T^{\,jet}\ |} = E_T^{\gamma} \cdot \sin\Delta\Phi. \tag{3}$$

  $\Delta\Phi$ is strongly correlated with $p_\perp$ but is less sensitive to the energies of the photon and the jet.

The y_h, E_T^{γ}, z and η^{jet} distributions of events with an isolated photon candidate are shown in figure 1 together with the MC predictions for the signal and the background. The signal (background) prediction is scaled by a factor 1.5 (1.7) in average, as suggested by the cross section measurement. The scaling factors vary for different wheels. In all distributions the data are described within errors by the scaled MC predictions. After the cut on the isolation of the photon there is still a significant contribution of background from the decay products of neutral mesons.

3.2 Photon Signal Extraction

The photon signal is extracted from the sample with photon candidates by means of a shower shape analysis, based on the method described in [15]. It uses the following six shower shape variables calculated from the measurements of the individual cells composing the cluster:

- The transverse radius of the cluster.
- The hottest cell fraction, the fraction of the energy of the electromagnetic cluster contained in the cell with the largest energy deposit.
- The hot core fraction, the fraction of the energy of the electromagnetic cluster contained in the hot core of the cluster.
- The first layer fraction, the fraction of the cluster's energy detected in the first calorimeter layer.
- The transverse symmetry of the cluster.
- The transverse kurtosis of the cluster

The distributions of the shower shape variables are shown in figure 2 for the prompt photon candidates. The shaded band shows the systematic uncertainty assigned to the description of the shower shapes. The data are compared with the sum of the background and the signal MC distributions, which describes the data within the systematic error.

In order to discriminate between signal and background, probability density functions p^i_γ and p^i_{bg} are defined for the six shower shape variables i. p^i_γ and p^i_{bg} are determined by using simulated events for the signal and the background.

The photon and background probability densities are taken as the product of the respective shower shape densities. For each event a discriminator (D) is formed. It is defined as the photon probability density divided by the sum of the probability densities for photons and background. Figure 3 shows the discriminator distribution for $0.94 < \eta^\gamma < 1.42$ and four different bins in E^γ_T. The data is shown together with the predictions of the background and the signal MC. The sum of the MC predictions describes the data within the systematic uncertainty of the shower shapes.

3.3 Cross Section Determination

A regularised unfolding procedure [16–18] is used to relate the measured observables $\vec{y}_{\text{obs}}$ to the true variables $\vec{x}_{\text{true}}$ on hadron level, determine the fraction of signal and background and to correct the data for the detector acceptance.

An unfolding matrix $\mathbf{A}$ which reflects the acceptance of the H1 detector relates the two vectors $\mathbf{A}\vec{x}_{\text{true}} = \vec{y}_{\text{obs}}$.

H1 Prompt Photon Phase Space	
Inclusive cross section	$6 < E_T^\gamma < 15$ GeV $-1. < \eta^\gamma < 2.43$ $z = E_T^\gamma / E_T^{\gamma-jet} > 0.9$ $Q^2 < 1$ GeV^2 $0.1 < y < 0.7$
Jet definition hadronic jet	k_T algorithm with P_T-weighted recombination scheme [14], $R_0 = 1$ $p_T^{\rm jet} > 4.5$ GeV $-1.3 < \eta^{\rm jet} < 2.3$

Table 1: Phase space for the measurement of isolated prompt photon cross sections. Kinematics are defined in the H1 laboratory frame.

The observables are E_T^γ and η^γ, each η^γ-E_T^γ bin is further divided into bins in $E_T^{\rm jet}$, $\eta^{\rm jet}$, x_γ^{LO}, x_p^{LO}, $\Delta\Phi$ or $p_\perp$ for the exclusive measurements. In addition, each measurement bin is binned in the discriminator D to allow the discrimination of signal and background.

The output contains the signal in bins $E_T^\gamma \times \eta^\gamma$on hadron level and the background in any of the input bins. For the exclusive measurement there is an additional binning in $E_T^{\rm jet}$, $\eta^{\rm jet}$, x_γ^{LO}, x_p^{LO}, $\Delta\Phi$ or $p_\perp$.

The unfolding matrix **A** is computed using the PYTHIA simulations for the signal and the background.

Cross sections are presented for $Q^2 < 1$ GeV^2. The extracted number of signal events in each bin N_{sig} is corrected for DIS events with a virtuality $1 < Q^2 < 4$ GeV^2, where the scattered electron escapes detection through the beam pipe. The correction factor f_{DIS} is determined with MC and is above 0.98.

4 Results

The prompt photon cross sections presented below are given for the phase space defined in table 1.

Bin averaged differential cross sections are presented in figures 4 to 8. The inner error bars of the measured cross section correspond to the uncorrelated errors, including the statistical error. The outer error bars include the correlated errors added in quadrature. For all measurements the total uncertainty is dominated by the systematic errors.

Theoretical uncertainties are estimated by varying μ_R and μ_F by 0.5 and 2.0. Different parton density functions change the theoretical predictions by $\pm 2\%$.

Differential cross sections $d\sigma/dE_T^\gamma$ and $d\sigma/d\eta^\gamma$ are presented in figure 4. The results are compared in figure 4 with the NLO pQCD calculation and the calculation based on the k_T factorisation approach. The soft underlying event activity reduces the total cross section by roughly

30% due to the isolation cut. The LZ calculation gives a nice description of the data, where FGH is below the data for backward photons ($\eta^\gamma < 0.2$). Figure 5 shows the double differential cross section $d\sigma/dE_T^\gamma d\eta^\gamma$ for all five bins in η^γ. The shape and the normalisation scale is described within errors by the predictions for $\eta^\gamma > -0.6$. For photons pointing backwards ($\eta^\gamma < 0.6$) FGH is low in normalisation.

The production of an isolated prompt photon together with a hadronic jet is also studied.

Cross sections for the production of a prompt photon and a hadronic jet are presented in figure 6 as a function of the variables E_T^γ, η^γ, E_T^{jet} and η^{jet}. The LZ calculation gives the best description of the η^γ and E_T^γ cross sections where the NLO calculation better describes E_T^{jet} and η^{jet} of the associated hadronic jet. Here, the LZ prediction is too high for jets with $\eta^{\text{jet}} < 0.5$.

The presence of a jet allows to define observables which give more insight in the underlying partonic process than for the inclusive case. Figure 7 shows the photon plus jet cross section as a function of the estimators x_γ^{LO} and x_p^{LO}. Whereas x_γ^{LO} is well described by both predictions, LZ is higher than the data at lowest x_p^{LO}.

Figure 8 shows the cross sections for two observables describing the transverse correlation between the photon and the jet, $p_\perp$ and $\Delta\Phi$. Both variables are particularly sensitive to higher order gluon emission. The sample is split into a sample with $x_\gamma^{LO} > 0.8$ (figures 8a and 8b) where the direct interaction of a photon with the proton dominates and a sample with $x_\gamma^{LO} < 0.8$ (figures 8c and 8d) with a significant contribution of events with a resolved photon. Both predictions slightly overestimate the back-to-back configuration for $x_\gamma^{LO} > 0.8$. For $x_\gamma^{LO} < 0.8$ there is a lower contribution from the back-to-back configuration, $p_\perp$ is significantly harder than for $x_\gamma^{LO} > 0.8$ and the photon tends to be closer to the jet. This reflects the increased contributions from events with a resolved photon and from photons radiated from quarks. FGH describes the distributions within the errors, except for the highest bin in $\Delta\Phi$ for $x_\gamma^{LO} < 0.8$. This region is sensitive to multiple soft gluon radiation which limits the validity of fixed order calculations [19]. The LZ calculation includes multiple soft gluon radiation in the initial state before the hard subprocess and describes $\Delta\Phi > 170°$ but predicts a significantly lower contribution of events with no back-to-back signature.

5 Conclusions

The photoproduction of prompt photons, both inclusively and associated with jets, is measured in ep collisions at a centre-of-mass energy of 319 GeV with the H1 detector at HERA using an integrated luminosity of $340\ \text{pb}^{-1}$. Photons with a transverse energy in the range $6 < E_T^\gamma < 15$ GeV and with pseudorapidity $-1.0 < \eta^\gamma < 2.43$ are measured in the kinematic region $Q^2 < 1\ \text{GeV}^2$ and $0.1 < y_h < 0.7$. Compared to previous measurements, the range of η^γ range is significantly extended.

The data are compared to a NLO calculation and to a calculation based on the k_T factorisation approach. For the inclusive sample the shapes of the $d\sigma/dE_T^\gamma$, $d\sigma/d\eta^\gamma$ and $d\sigma/dE_T^\gamma d\eta^\gamma$ distributions are described within errors, except for $\eta^\gamma < -0.6$ where the NLO prediction is significantly below the data.

For the exclusive sample of a photon associated with a jet, differential cross sections are measured as a function of E_T^γ, η^γ, $\eta^{\rm jet}$, $E_T^{\rm jet}$ and x_γ^{LO} and x_p^{LO}, which in LO correspond to the longitudinal momentum fractions of the partons in the photon and the proton, respectively. The LZ calculation gives the best description of the η^γ and E_T^γ cross sections where the NLO calculation better describes $E_T^{\rm jet}$ and $\eta^{\rm jet}$ of the associated hadronic jet.

Transverse correlations between the jet and the photon are investigated by measurements of the difference in azimuthal angle $\Delta\Phi$ and the photon momentum transverse to the jet direction $p_\perp$. A significant fraction of events for $x_\gamma^{LO} < 0.8$ shows a topology which is not back-to-back. It is well described by the NLO calculation, while the k_T factorisation predicts a too soft $p_\perp$ distribution.

Acknowledgements

We are grateful to the HERA machine group whose outstanding efforts have made this experiment possible. We thank the engineers and technicians for their work in constructing and maintaining the H1 detector, our funding agencies for financial support, the DESY technical staff for continual assistance and the DESY directorate for support and for the hospitality which they extend to the non DESY members of the collaboration. We would like to thank Artem Lipatov and Nikolai Zotov for providing the LZ calculations and Gudrun Heinrich for help with the FGH calculations.

References

[1] A. Aktas *et al.* [H1 Collaboration], "Measurement of prompt photon cross sections in photoproduction at HERA," Eur. Phys. J.**C38** (2005) 437 [hep-ex/0407018].

[2] M. Fontannaz, J. P. Guillet and G. Heinrich, "Isolated prompt photon photoproduction at NLO," Eur. Phys. J. C **21** (2001) 303 [hep-ph/0105121].

[3] M. Fontannaz and G. Heinrich, "Isolated photon + jet photoproduction as a tool to constrain the gluon distribution in the proton and the photon," Eur. Phys. J. C **34**, 191 (2004) [hep-ph/0312009].

[4] J. Pumplin, D. R. Stump, J. Huston, H. L. Lai, P. Nadolsky and W. K. Tung, "New generation of parton distributions with uncertainties from global QCD analysis," JHEP **0207** (2002) 012 [hep-ph/0201195].

[5] P. Aurenche, J. P. Guillet and M. Fontannaz, "Parton distributions in the photon," Z. Phys. C **64** (1994) 621 [hep-ph/9406382].

[6] A. V. Lipatov and N. P. Zotov, "Prompt photon photoproduction at HERA in the k(T)-factorization approach," Phys. Rev. D **72** (2005) 054002 [hep-ph/0506044].

[7] M. A. Kimber, A. D. Martin and M. G. Ryskin, "Unintegrated parton distributions," Phys. Rev. D **63** (2001) 114027 [hep-ph/0101348].

[8] M. Glück, E. Reya and A. Vogt, “Photonic Parton Distributions,” Phys. Rev. D **46** (1992) 1973.

[9] M. Glück, E. Reya and A. Vogt, “Dynamical Parton Distributions Of The Proton And Small X Physics,” Z. Phys. C **67** (1995) 433.

[10] T. Sjöstrand *et al.*, PYTHIA 6.2 Physics and Manual [hep-ph/0108264].

[11] G. A. Schuler and T. Sjostrand, “Parton Distributions of the Virtual Photon,” Phys. Lett. B **376** (1996) 193 [hep-ph/9601282].

[12] R. Brun *et al.*, “GEANT 3” CERN_DD/EE/84-1.

[13] I. Abt *et al.*, “The H1-Detector at HERA,” Nucl. Instr. and Meth. **A 386** (1997) 310; ibid, 348.

[14] S. D. Ellis and D. E. Soper, “Successive combination jet algorithm for hadron collisions,” Phys. Rev. D **48** (1993) 3160 [arXiv:hep-ph/9305266].

[15] F.D.Aaron *et al.* [H1 Collaboration], “Measurement of isolated photon production in deep-inelastic scattering at HERA,” Eur. Phys. J. **C54** (2008) 371 [arXiv:0711.4578 [hep-ex]].

[16] D. L. Phillips, “A technique for the numerical solution of certain integral equations of the first kind,” J. Assoc. Comput. Mach, **9** (1962) 84.

[17] A. N. Tikhanov, “Solution of incorrectly formulated problems and the regularization method,” Soviet Math. Dokl., **4** (1963) 1035; English translation of Dokl. Akad. Nauk. SSSR, **151** (1963) 501.

[18] V. Blobel, “An unfolding method for high energy physics experiments,” Proc. Advanced Statistical Techniques in Particle Physics, Durham (2002).

[19] Gudrun Heinrich, private communication.

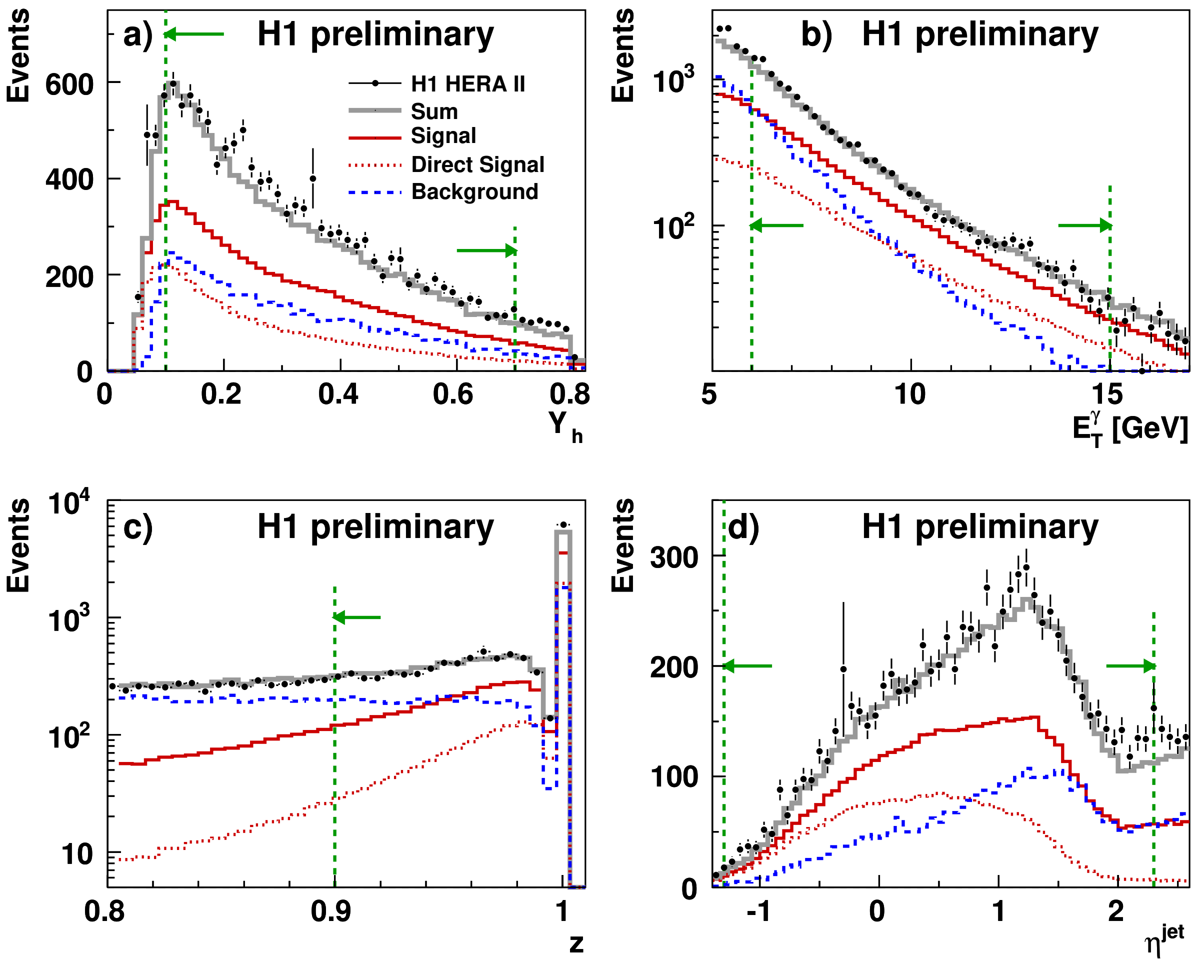

Figure 1: Distributions of (a) the inelasticity y_h, (b) the transverse energy E_T^{γ} of the photon, (c) the isolation parameter z and (d) E_T^{jet} for events with prompt photon candidates. Data are shown as points with error bars indicating the statistical error. The signal is shown as full line, the contribution of direct interactions as dotted line. The background is shown as dashed line. The signal and background contributions are scaled according to the cross section measurement. The sum of the scaled signal and background is shown as the light grey histogram. The vertical dashed lines indicate the kinematic region of the cross section measurement.

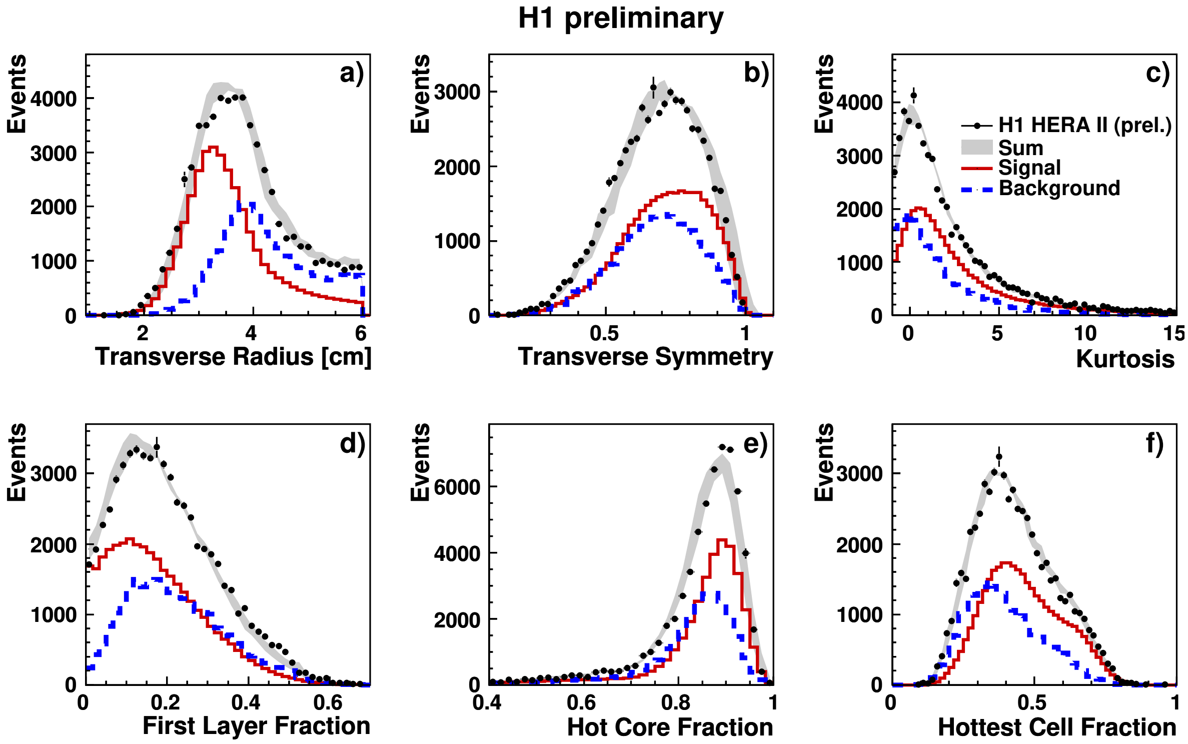

Figure 2: Distributions of the shower shape variables that are used to define the discriminant for isolated photon identification: (a) transverse radius (R_T), (b) transverse symmetry, (c) transverse kurtosis (d) the fraction of energy in the first layer, (e) the fraction of energy in the hot core of the cluster and (f) the fraction of energy in the hottest cell of the cluster for all the photon candidates. Data are shown as points with error bars for the statistical error. The expectation from PYTHIA for the signal (background) is shown as full (dashed) line. The signal and background contributions are scaled according to the cross section measurement. The shaded band shows the sum of the MC predictions, the width of the band corresponds to the systematic uncertainty assigned to the description of the shower shapes.

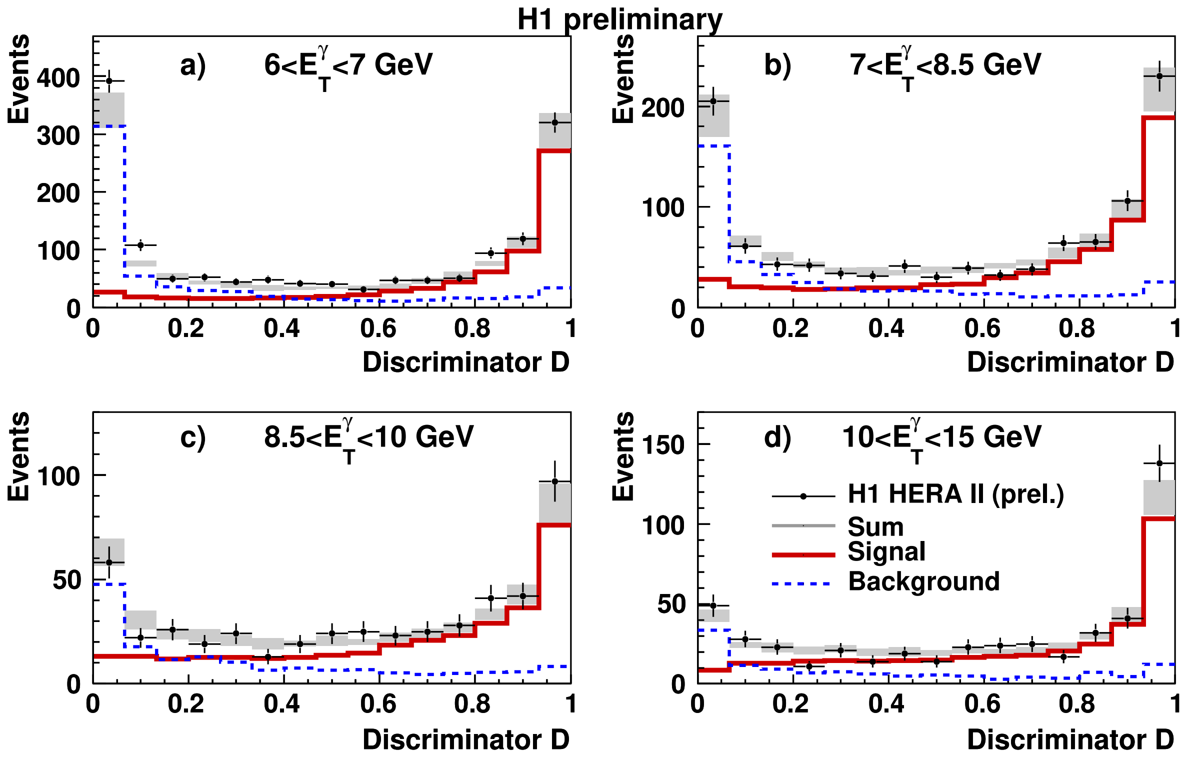

Figure 3: The distribution of the discriminant D for $0.94 < \eta^{\gamma} < 1.42$ in four different E_T^{γ} bins. D is used in the identification of prompt photon candidates for events that have passed the event selection. Data are shown as points with error bars for the statistical error. The expectiation from PYTHIA for the signal (background) is shown as full (dashed) line. The signal and background contributions are scaled according to the cross section measurement. The shaded band shows the sum of the MC predictions with the systematic uncertainty assigned to the description of the shower shapes.

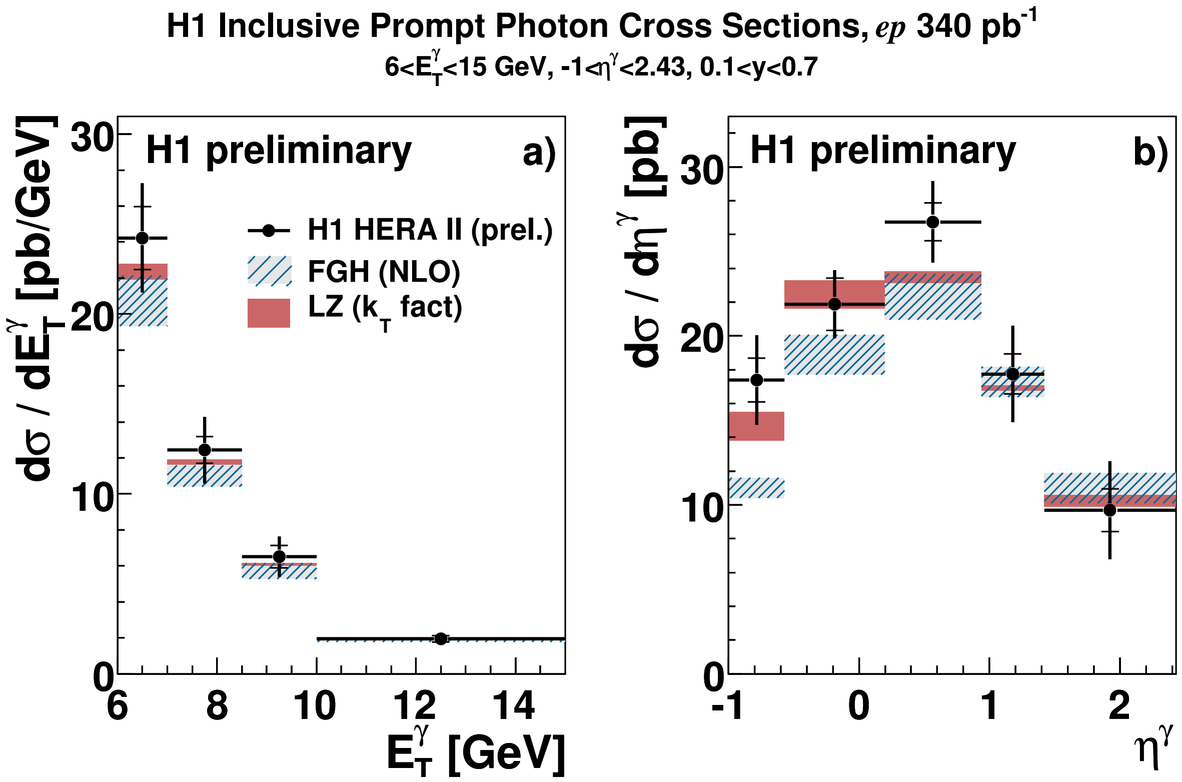

Figure 4: Inclusive differential prompt photon cross sections $d\sigma/dE_T^\gamma$ (a) and $d\sigma/d\eta^\gamma$ (b) in the kinematic range specified in table 1. The inner error bars on the data points indicate the correlated error, the full error bars contain in addition the uncorrelated errors added in quadrature. The data is compared to to a NLO pQCD calculation and to a calculation based on the $k_t$factorisation approach. For each plot the lower figure shows the ratio of the measured cross section (σ_{meas}) to the predicted FGH cross section ($R = \sigma_{meas}/\sigma_{FGH}$, the error is given by the correlated error. The uncorrelated error is indicated by the shaded area between the dashed and dotted lines, the hatched area shows the relative error of the NLO calculation.

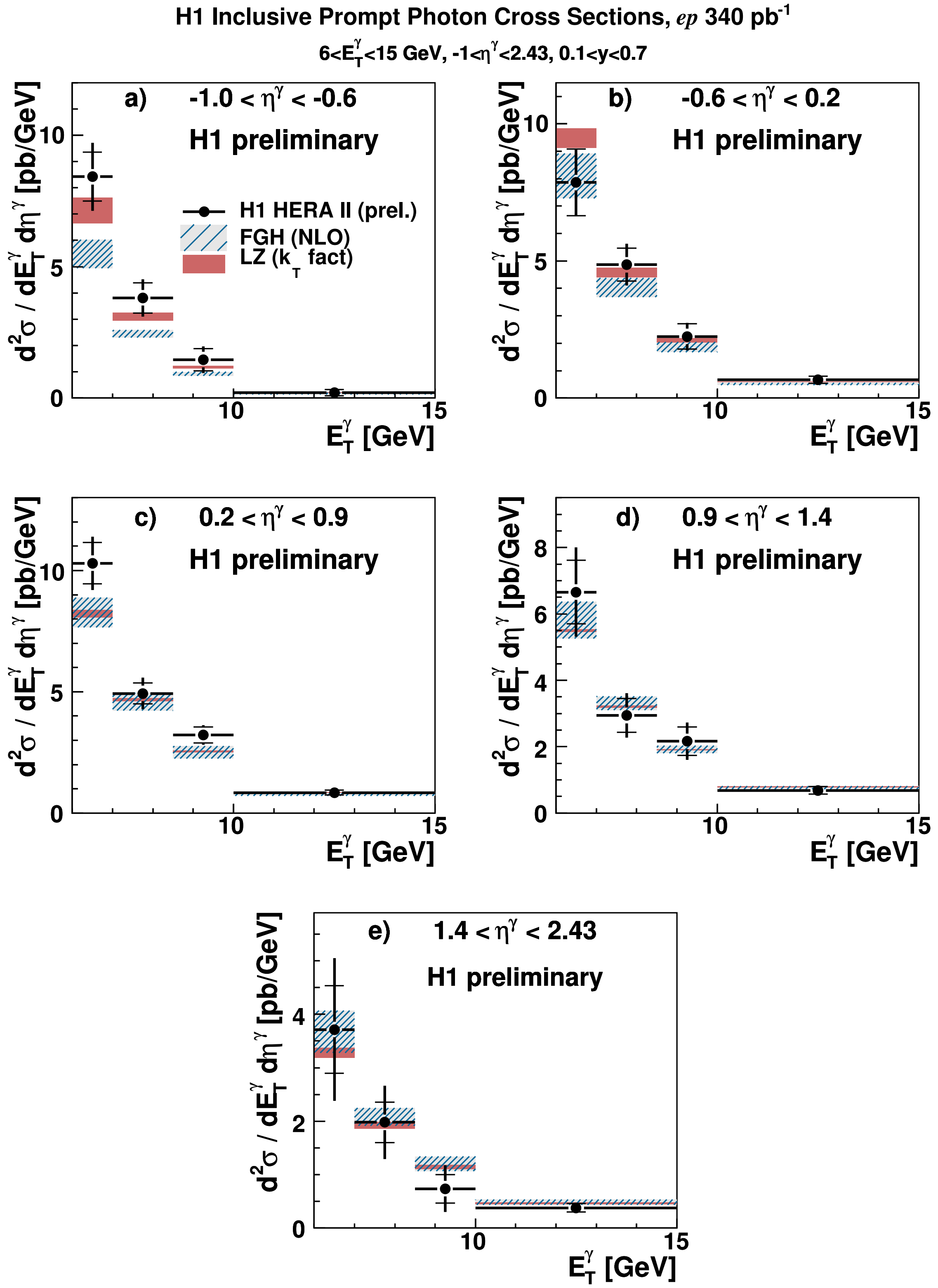

Figure 5: Inclusive double differential prompt photon cross sections $d\sigma/dE_T^\gamma d\eta^\gamma$ for five bins in η^γcorresponding to the wheel structure of the LAr calorimeter. The errors between different η^γ bins are correlated. The kinematic range is specified in table 1. The cross sections are compared to theoretical calculations as in figure 4.

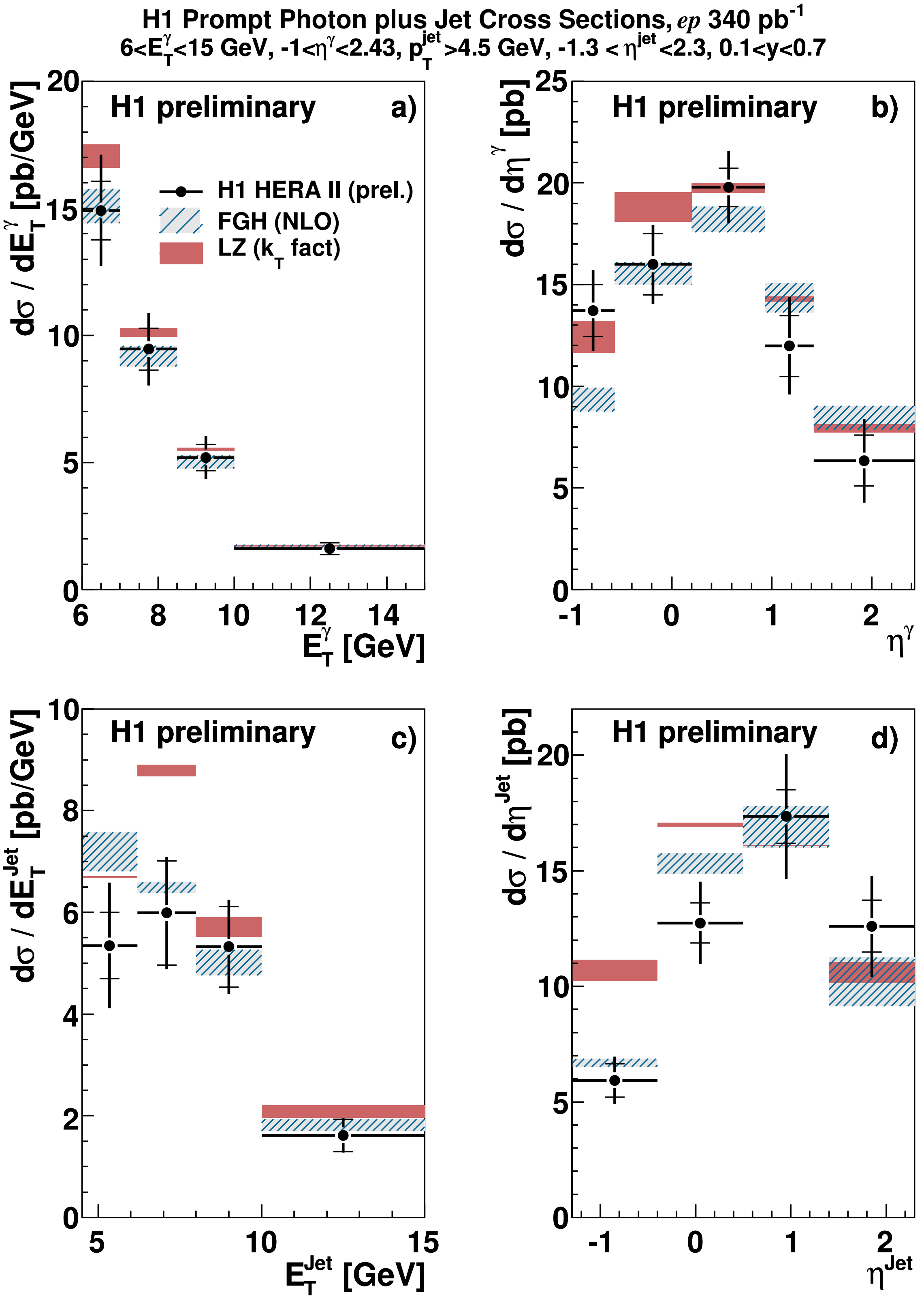

Figure 6: Differential prompt photon plus jet cross sections $d\sigma/d\eta^{\gamma}$ (a), $d\sigma/dE_T^{\gamma}$ (b), $d\sigma/d\eta^{\rm jet}$ (c) and $d\sigma/dE_T^{\rm jet}$ (d) in the kinematic range specified in table 1. The cross sections are compared to theoretical calculations as in figure 4.

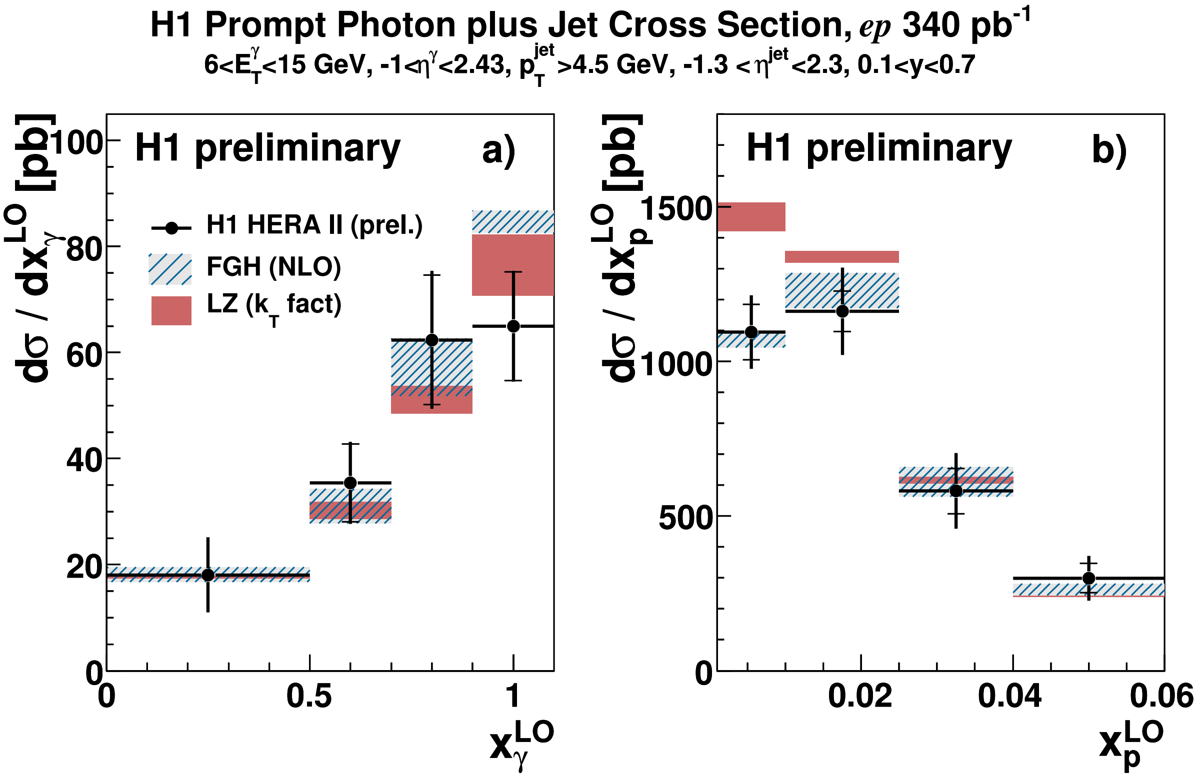

Figure 7: Differential prompt photon plus jet cross sections $d\sigma/dx_{\gamma}^{LO}$ (a), $d\sigma/dx_{p}^{LO}$ (b), in the kinematic range specified in table 1. The cross sections are compared to theoretical calculations as in figure 4.

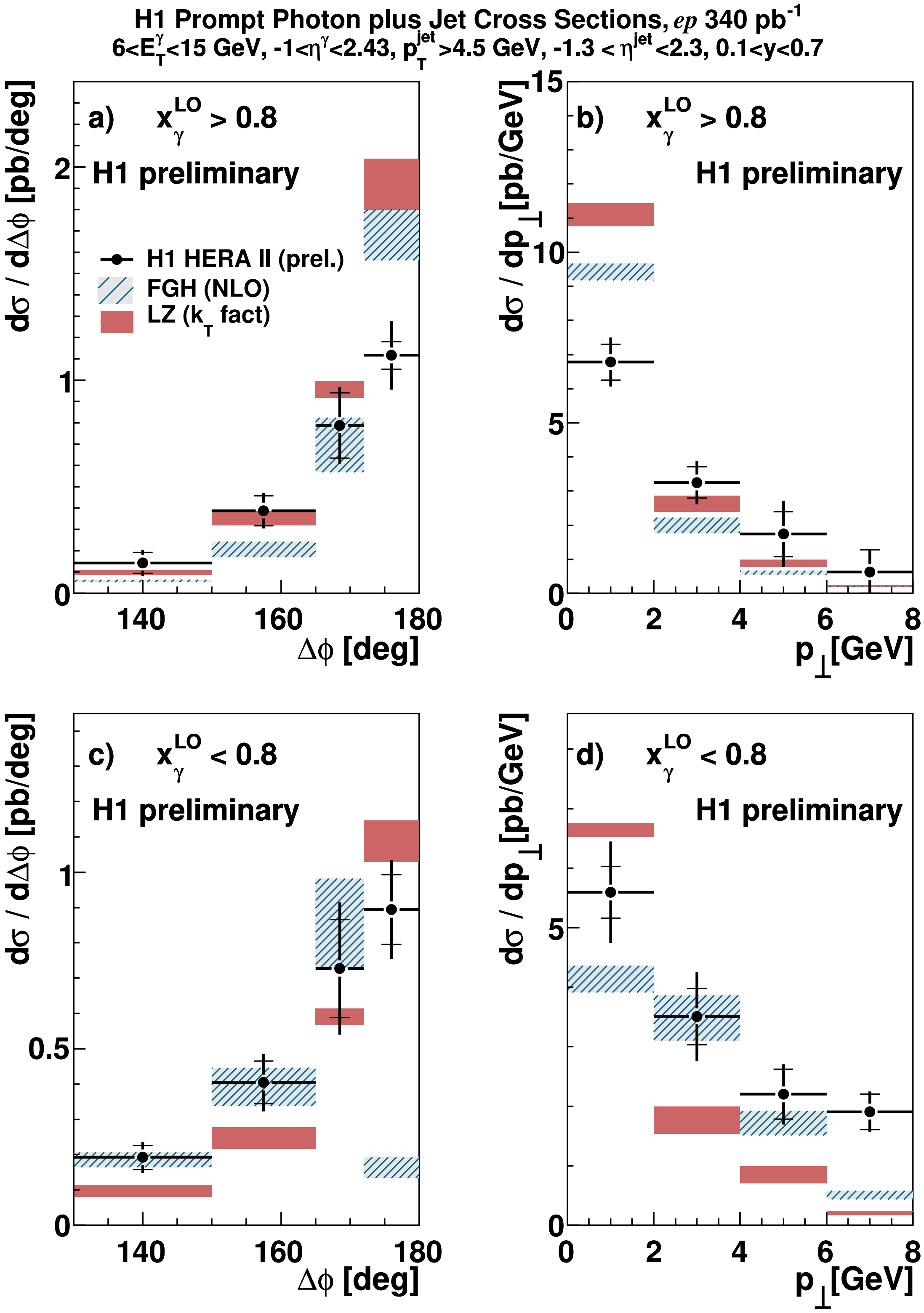

Figure 8: Differential prompt photon plus jet cross sections $d\sigma/d\Delta\Phi$ (a and c) and $d\sigma/dp_\perp$ (b and d) the photon momentum transverse to the jet direction the difference in azimuthal angle between the photon and the jet in the kinematic range specified in table 1. (a) and (b) show the cross section for $x_\gamma^{LO} > 0.8$, (c) and (d) for $x_\gamma^{LO} < 0.8$. The cross sections are compared to theoretical calculations as in figure 4.